Research Article | Vol. 24, No. 25 | 12 Dec 2016 | OPTICS EXPRESS 28889

Optics EXPRESS

# Modeling framework for piezoelectrically actuated MEMS tunable lenses

MAHMOUD A. FARGHALY, MUHAMMAD NADEEM AKRAM, AND EINAR HALVORSEN*

*Department of Micro- and Nanosystem Technology, University College of Southeast Norway, Norway*
*Einar.Halvorsen@hbv.no

**Abstract:** We report a modeling framework for evaluating the performance of piezoelectrically actuated MEMS tunable lenses. It models the static opto-electromechanical coupling for symmetric configurations of piezoelectric actuators based on the laminated-plate theory, linear piezoelectricity, and ray tracing. With these assumptions, it helps to find geometrical parameters for actuators on clamped square or circular diaphragms that give a diffraction-limited tunable lens with minimum F-number. The tunable lens' optical performance and its focusing capability, alone and in combination with a paraxial fixed lens, were calculated in terms of object distance and actuation voltage. Using the modeling framework, we confirmed that the modulation transfer function for objects located at different distances remains the same after voltage adjustment.



**OCIS codes:** (230.0230) Optical devices; (230.3990) Micro-optical devices; (230.4685) Optical microelectromechanical devices; (110.0110) Imaging systems; (110.1080) Active or adaptive optics.

## References and links

1. Y. Tseng, "Voice coil motor apparatus," US Patent 7,400,068 (2008).
2. C. Zhao, *Ultrasonic Motors: Technologies and Applications* (Science Press Beijing and Springer-Verlag Berlin Heidelberg, 2011).
3. M. Ye, B. Wang, and S. Sato, "Liquid-crystal lens with a focal length that is variable in a wide range," Appl. Opt. **43**, 6407–6412 (2004).
4. N. Chronis, G. Liu, K.-H. Jeong, and L. Lee, "Tunable liquid-filled microlens array integrated with microfluidic network," Opt. Express **11**, 2370–2378 (2003).
5. A. Werber and H. Zappe, "Tunable microfluidic microlenses," Appl. Opt. **44**, 3238–3245 (2005).
6. S. Kuiper, B. H. Hendriks, L. J. Huijbregts, A. M. Hirschberg, C. A. Renders, and M. A. van As, "Variable-focus liquid lens for portable applications," Proc. SPIE **5523**, 100–109 (2004).
7. U. Wallrabe, "Axicons et al. - highly aspherical adaptive optical elements for the life sciences," in "2015 18th International Conference on Solid-State Sensors, Actuators and Microsystems (TRANSDUCERS), 2015 Transducers," (2015), pp. 251–256.
8. K. Haugholt, D. Wang, F. Tyholdt, W. Booij, and I. Johansen, "Polymer lens," US Patent 8,199,410 (2012).
9. V. N. Mahajan, "Zernike circle polynomials and optical aberrations of systems with circular pupils," Appl. Opt. **33**, 8121–8124 (1994).
10. M. Deshpande and L. Saggere, "An analytical model and working equations for static deflections of a circular multi-layered diaphragm-type piezoelectric actuator," Sensors and Actuators A: Physical **136**, 673–689 (2007).
11. S. I. E. Lin, "Investigation on packaging parameters of a circular multi-layered diaphragm-type piezoelectric actuator," Computers and Structures **89**, 371–379 (2011).
12. J. N. Reddy, *Mechanics of Laminated Composite Plates and Shells: Theory and Analysis*, 2nd ed. (CRC Press, 2004).
13. J. F. Nye, *Physical Properties of Crystals: Their Representation by Tensors and Matrices* (Oxford University Press, 1985).
14. V. Birman, *Plate Structures*, vol. 178 of *Solid Mechanics and its Applications* (Springer Science+Bussiness Media, 2011).
15. E. Tadmor and G. Kosa, "Electromechanical coupling correction for piezoelectric layered beams," Journal of Microelectromechanical Systems **12**, 899–906 (2003).
16. H. F. Tiersten, "Hamilton's principle for linear piezoelectric media," in *Proceedings of the IEEE* **55** (IEEE, 1967), pp. 1523–1524.
17. J. Reddy and J. Mitchell, "On refined nonlinear theories of laminated composite structures with piezoelectric laminae," Sadhana **20**, 721–747 (1995).
18. J. W. Goodman, *Introduction to Fourier Optics* (McGraw-Hill, 1996).
19. P. Laura, E. Romanelli, and R. Rossi, "Transverse vibrations of simply supported rectangular plates with rectangular cutouts," Journal of Sound and Vibration **202**, 275–283 (1997).

#278094 http://dx.doi.org/10.1364/OE.24.028889
Journal © 2016 Received 6 Oct 2016; accepted 29 Nov 2016; published 6 Dec 2016

Optics EXPRESS

20. B. Boyerinas, C. Mo, and W. W. Clark, "Behavior of unimorph rectangular piezoelectric diaphragm actuators," Proc. SPIE **6173**, 617302 (2006).
21. R. L. Taylor and S. Govindjee, "Solution of clamped rectangular plate problems," Communications in Numerical Methods in Engineering **20**, 757–765 (2004).
22. F. W. J. Olver, D. W. Lozier, R. F. Boisvert, and C. W. Clark, *NIST Handbook of Mathematical Functions* (Cambridge Univeristy Press, New York, 2010).
23. N. Ledermann, P. Muralt, J. Baborowski, S. Gentil, K. Mukati, M. Cantoni, A. Seifert, and N. Setter, "1 0 0-textured, piezoelectric $Pb(Zr_xTi_{1-x})O_3$ thin films for MEMS: integration, deposition and properties," Sensors and Actuators A: Physical **105**, 162–170 (2003).
24. T. Bakke, A. Vogl, O. Żero, F. Tyholdt, I.-R. Johansen, and D. Wang, "A novel ultra-planar, long-stroke and low-voltage piezoelectric micromirror," Journal of Micromechanics and Microengineering **20**, 064010 (2010).
25. Zemax LLC, *Zemax User's Manual* (2015).
26. A. Maréchal, "Etude des influences conjuguées des aberrations et de la diffraction sur l'image d'un point," Ph.D. thesis, Faculté des Sciences des Paris (1947).

## 1. Introduction

Autofocus is a crucial feature in cameras, especially when photographing objects at different distances and having them in sharp focus without any quality loss in the captured image. Over the last decades, several research efforts have been made to incorporate tunable focus for mobile-device cameras using micro-scale components. Qualitatively, this enables miniaturized cameras with lower power consumption, much faster response in scanning focus range and higher reliability. The microelectromechanical-systems-(MEMS)-based tunable focus lenses are promising alternatives as autofocus mechanisms when compared to the conventional macro-scale approaches such as the voice coil motor (VCM) [1] or ultrasonic motor [2]. Moreover, such MEMS autofocus lenses will achieve higher resolution smartphone cameras without any moving parts within the camera housing, which consume power during focus adjustment and causes a loss in the field of view as for the VCM.

In conventional macro-scale focusing systems sold in the camera market nowadays, for example VCM and ultrasonic motors, tunable focus is achieved through changing the relative positions of lenses mounted inside a barrel in front of a fixed lens. Each technology moves that barrel differently within the camera housing. The VCM effectively uses Lorentz forces on current carrying coils wrapped around the barrel to move it forwards or backwards. Ultrasonic motors use piezoelectric actuators to generate a traveling wave rotating along the circumference of a circular disk and couple the resultant circular movement through a gear system to an axially moving lever attached to the barre.

Tunable focus in micro-scale systems is generally achievable by two approaches. The first approach is to change the effective refractive index as in a liquid crystal (LC) lens [3]. An LC lens can converge or diverge light beams by controlling the electric field that reorients LC molecules causing a spatially dependent refractive index within LC layers. The second approach is to change the interface slope through which the light rays are passing between two media with different refractive indices. Tunable microfluidic lenses [4, 5] can use a pump to control the pressure of a liquid trapped inside a fluidic cavity to deform the cavity's top surface. A tunable liquid lens changes the interface curvature between two polar liquids by electrowetting [6]. Piezoelectrically actuated lenses bend a transparent membrane between two media with different refractive indices to provide a spatially dependent slope at the interface. The media can be air and a fluid [7], or air and a polymer as in the TLens® case [8].

In this article, we introduce a modeling framework that predicts the static opto-electromechanical coupling of different electrode configurations for piezoelectrically actuated MEMS tunable lenses. The static electromechanical performance is modeled based on variational methods for square diaphragms. Simple analytical formulas are used for circular diaphragms. To solve the variational formulation, we found a basis that is practical for calculation of the resulting variational integrals and that can be simply expressed in terms of Zernike polynomials [9] which

are convenient for wavefront representations in optical simulations. We provide closed forms for the variational integrals that simplify the numerical calculations for large numbers of basis functions. We have investigated the tunable lens's optical performance using ray tracing by analysing its $F$-number ($F\#$), RMS wavefront error and Modulation Transfer Function (MTF). The MTF response of the tunable lens in combination with a paraxial fixed lens remains essentially the same when the object is located at different distances after actuation voltage adjustment.

## 2. Principle of operation

The MEMS tunable lenses that we study here are based on piezoelectric actuation as a bending mechanism of a diaphragm to provide a voltage dependent curvature at the interface between air and a polymer [8] or air and a fluid [7]. In the paraxial approximation for a thin plano-convex lens with radius of curvature $R$ and refractive index $n_{\text{medium}}$, the focal length is $f = R/(n_{\text{medium}} - 1)$. The lens shown in Fig. 1 consists of four elements: a piezoelectric actuator, a thin transparent glass layer, a soft polymer gel (or fluid) and a transparent thicker glass layer as substrate. A DC voltage $V_{\text{p}}$ is applied to the piezoelectric actuator to set an electric field $E_3$ having the same alignment as the polarization within the piezoelectric material. This causes an in-plane contraction in the piezoelectric stack and the flexible thin glass layer bends upwards. The upper surface of the soft polymer (or fluid) is shaped by this bending, forming a complicated refractive surface for light rays, as shown in Fig. 1. Thus, controlling the actuation voltage $V_{\text{p}}$ makes the lens's focusing-power tunable and enables focusing at objects located at different distances from the camera. This tunable lens could be attached to a fixed-focal-length optical system (*e.g.* a smartphone camera) for adjusting the overall focal length based on the object distance from the photographing device.

Figure 2 shows a planar view of different possible study cases for the tunable lenses. For all cases, light should only pass through the circular opening. Thus, cases (II, IV) with ring actuators have an additional opaque area (*i.e.* the lower Pt electrode of the piezoelectric stack) covering the diaphragm outside the actuator perimeter till the diaphragm edge in order to block out light.

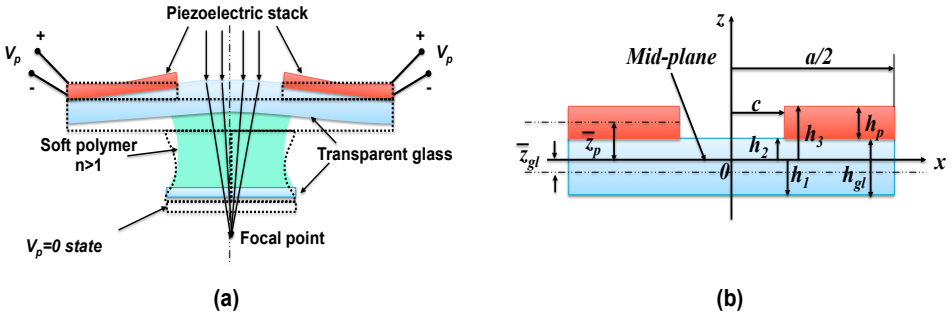


Fig. 1. (a) Schematic view showing tunable lens's principle of operation; both at rest position when $V_{\text{p}} = 0$ and at focus when $V_{\text{p}}$ is nonzero. (b) Cross-sectional view of tunable lens showing dimensions.

## 3. Electromechanical modeling and simulations

This section describes the models that are used to predict the deformed shape of the transparent membrane. For the square diaphragms, we have developed a variational formulation. For the circular diaphragms, we use simple analytical formulas [10, 11]. For the cases of interest, it is reasonable to use Classical Laminated Plate Theory (CLPT) since the in-plane diaphragm dimension $a$ is larger than its thickness.

Optics EXPRESS

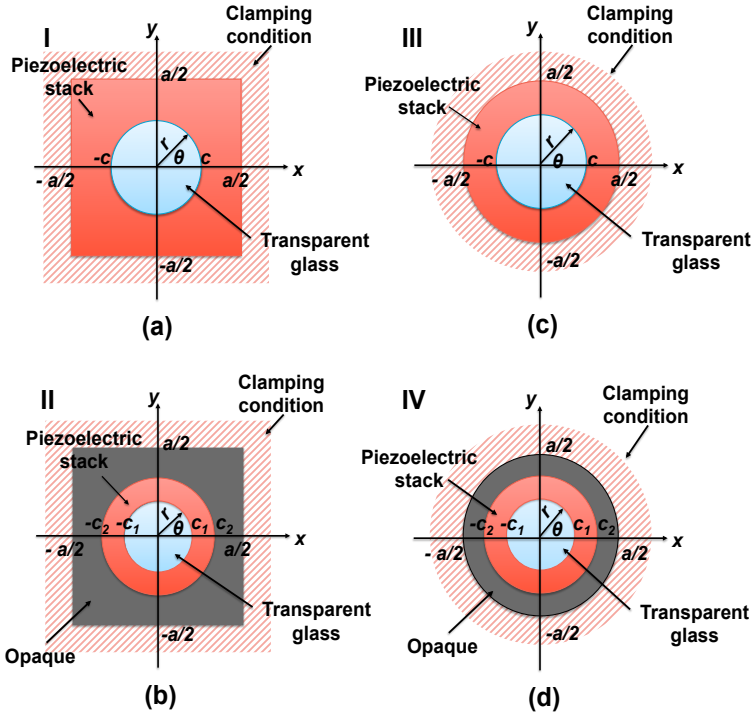


Fig. 2. Planar view of possible study cases of piezoelectrically actuated MEMS tunable lenses. A clamped square diaphragm with circular opening: (a) case I and (b) case II ring actuator with opaque covering outside the ring till the diaphragm edges. A clamped circular diaphragm with circular opening: (c) case III actuator and (d) case IV ring actuator with opaque covering outside the ring till the diaphragm edges.

### 3.1. *Square diaphragm*

The core of our modeling framework for square diaphragms is a weak formulation based on six assumptions. First, CLPT [12] which takes into account only first order strains but neglects the transverse shear engineering strains $\gamma_{xz}$ and $\gamma_{yz}$. Second, the linear theory of piezoelectricity that assumes a linear coupling between electric field components and strains. Third, the piezoelectric layer is a charge free region so that Gauss's law simplifies to $\nabla \cdot \mathbf{D} = 0$. Fourth, quasi-electrostatic conditions such that there is no time dependence. Fifth, a thin film approximation which neglects the lack of smoothness at the transitions between areas that are covered by a piezoelectric thin film and those that aren't. This approximation is made by using an orthogonal basis that is continuous and differentiable over the whole diaphragm plane. Sixth, the medium that is deformed by actuation of the diaphragm is assumed to be weightless and not to affect the diaphragm bending. This applies whether the medium is a soft polymer as in the TLens device or a fluid-filled cavity.

Optics EXPRESS

#### 3.1.1. Constitutive equations

For a $\infty mm$ [13] piezoelectric material, the constitutive equations referred to the middle plane as a reference plane (referring to Fig. 1(b)) can be reduced to

$$\begin{bmatrix} T_{xx} \\ T_{yy} \\ T_{xy} \\ D_3 \end{bmatrix} = \begin{bmatrix} \overline{Q}_{11} & \overline{Q}_{12} & 0 \\ \overline{Q}_{12} & \overline{Q}_{22} & 0 \\ 0 & 0 & \overline{Q}_{66} \\ \overline{e}_{31} & \overline{e}_{32} & 0 \end{bmatrix} \begin{bmatrix} S_{xx} \\ S_{yy} \\ \gamma_{xy} \end{bmatrix} - \begin{bmatrix} \overline{e}_{31} \\ \overline{e}_{32} \\ 0 \\ \overline{\epsilon}^S_{33} \end{bmatrix} E_3 \tag{1a}$$

$$\begin{bmatrix} D_1 \\ D_2 \end{bmatrix} = \begin{bmatrix} \overline{e}_{15} & 0 \\ 0 & \overline{e}_{24} \end{bmatrix} \begin{bmatrix} \gamma_{yz} \\ \gamma_{xz} \end{bmatrix} + \begin{bmatrix} \overline{\epsilon}^S_{11} & 0 \\ 0 & \overline{\epsilon}^S_{22} \end{bmatrix} \begin{bmatrix} E_1 \\ E_2 \end{bmatrix} \tag{1b}$$

where $T_{ij}$, $S_{ij}$, $\gamma_{ij}$, $D_i$ and $E_i$ are components of stress, normal strain, shear strain, electric displacement and electric field respectively. ($\overline{Q}_{ij}$, $\overline{e}_{ij}$, $\overline{\epsilon}^S_{ij}$) are effective material properties, defined in the Appendix. The material axes (1, 2 and 3) coincide with the coordinate axes ($x$, $y$ and $z$). $D_1$ and $D_2$ can be neglected due to negligible transverse shear strains ($\gamma_{xz}$ and $\gamma_{yz}$) and zero $E_1$ and $E_2$ from the electrode configuration.

It is useful to integrate Eq. (1a) over the thickness to get expressions for the stress resultants as follows [12, 14]

$$\begin{bmatrix} N_{xx} \\ N_{yy} \\ N_{xy} \\ M_{xx} \\ M_{yy} \\ M_{xy} \end{bmatrix} = \begin{bmatrix} A_{11} & A_{12} & 0 & B_{11} & B_{12} & 0 \\ A_{12} & A_{22} & 0 & B_{21} & B_{22} & 0 \\ 0 & 0 & A_{66} & 0 & 0 & B_{66} \\ B_{11} & B_{12} & 0 & D_{11} & D_{12} & 0 \\ B_{12} & B_{22} & 0 & D_{21} & D_{22} & 0 \\ 0 & 0 & B_{66} & 0 & 0 & D_{66} \end{bmatrix} \begin{bmatrix} S^0_{xx} \\ S^0_{yy} \\ \gamma^0_{xy} \\ S^1_{xx} \\ S^1_{yy} \\ \gamma^1_{xy} \end{bmatrix} - \begin{bmatrix} N^E_{xx} \\ N^E_{yy} \\ N^E_{xy} \\ M^E_{xx} \\ M^E_{yy} \\ M^E_{xy} \end{bmatrix} \tag{2}$$

where

$$A_{ij} = \sum_{k=1}^{2} \overline{Q}^{(k)}_{ij}(h_{k+1} - h_k), \quad B_{ij} = \frac{1}{2}\sum_{k=1}^{2} \overline{Q}^{(k)}_{ij}(h^2_{k+1} - h^2_k) \quad \text{and} \quad D_{ij} = \frac{1}{3}\sum_{k=1}^{2} \overline{Q}^{(k)}_{ij}(h^3_{k+1} - h^3_k).$$

$\overline{Q}^{(k)}_{ij}$ are the effective stiffness coefficients for the $k^{th}$ layer and ($i$, $j$=1, 2, 6). ($S^0_{ii}$, $\gamma^0_{xy}$) and ($S^1_{ii}$, $\gamma^1_{xy}$) are membrane stretching strains at middle surface and bending (flexural) strains [12]. $N_{ij}$ and $M_{ij}$ are the thickness integrated forces and moments, respectively. $N^E_{ij}$ and $M^E_{ij}$ identified by a superscript $E$ are terms that originate from the piezoelectric coupling [14]. From Gauss's law and electric boundary conditions ($v = 0$ at ($z = h_2$) and $v = V_\mathrm{p}$ at ($z = h_3$)), we can formulate expressions for $E_3$ and the voltage $v$ in terms of the bending strains, the DC actuation voltage $V_\mathrm{p}$ and layers dimensions (refer to Fig. 1) as

$$E_3(x, y, z) = \frac{-V_\mathrm{p}}{h_\mathrm{p}} - \frac{\overline{e}_{31}}{\epsilon^S_{33}}\left(S^1_{xx} + S^1_{yy}\right)(z - \overline{z}_\mathrm{p}), \tag{3a}$$

$$v(x, y, z) = \frac{V_\mathrm{p}}{h_\mathrm{p}}(z - h_2) + \frac{\overline{e}_{31}}{\epsilon^S_{33}}\left(S^1_{xx} + S^1_{yy}\right)\left(\frac{(z^2 - h^2_2)}{2} + \overline{z}_\mathrm{p}(h_2 - z)\right) \tag{3b}$$

where $\overline{z}_\mathrm{p} = (h_2 + h_3)/2$.

The first term on the right hand side of Eqs. (3) is the field one would have without deformation and the second term is a result of the deformation through the piezoelectric coupling. Thus, we can express the thickness integrated forces and moments of a piezoelectric origin as

$$N^E_{xx} = N^E_{yy} = -\overline{e}_{31}V_\mathrm{p}, \quad N^E_{xy} = 0, \tag{4a}$$

$$M^E_{xx} = M^E_{yy} = -\overline{e}_{31}\left[\frac{\overline{e}_{31}}{\epsilon^S_{33}}\left(S^1_{xx} + S^1_{yy}\right)\left(\frac{(h_3 - h_2)^3}{12}\right) + V_\mathrm{p}\overline{z}_\mathrm{p}\right], \quad M^E_{xy} = 0. \tag{4b}$$

Optics EXPRESS

Since the deflection is dominated by diaphragm bending, we will neglect the stretching strains at the middle surface ($S^0_{xx}$, $S^0_{yy}$ and $\gamma^0_{xy}$). This will decouple the cross terms between the thickness integrated forces and moments in Eq. (2). By backsubstituting from Eqs. (4) into Eq. (2), we get the thickness-integrated moments

$$\begin{bmatrix} M_{xx} \\ M_{yy} \\ M_{xy} \end{bmatrix} = \begin{bmatrix} D^*_{11} & D^*_{12} & 0 \\ D^*_{21} & D^*_{22} & 0 \\ 0 & 0 & D^*_{66} \end{bmatrix} \begin{bmatrix} S^1_{xx} \\ S^1_{yy} \\ \gamma^1_{xy} \end{bmatrix} + \overline{e}_{31} V_p \overline{z}_\mathrm{p} \begin{bmatrix} 1 \\ 1 \\ 0 \end{bmatrix} \tag{5}$$

where

$$D^*_{ij} = D^{\mathrm{gl}}_{ij} + D^{\mathrm{p}}_{ij} = \sum_{k=1}^{2} \overline{Q}^{(k)}_{ij} \left[ \frac{1}{12} \left( 1 + \chi^{(k)}_{ij} \right) (h_{k+1} - h_k)^3 \right] \text{ and } \chi^{(k)}_{ij} = \frac{\overline{e}^{(k)}_{3i} \overline{e}^{(k)}_{3j}}{\overline{Q}^{(k)}_{ij} \overline{\epsilon}^{S;(k)}_{33}}.$$

$D^*_{ij}$ are modified membrane flexural stiffnesses, $D^{\mathrm{gl}}_{ij}$ is for the glass layer only, $D^{\mathrm{p}}_{ij}$ for the piezoelectric layer only and $\chi_{ij}$ is a correction factor to the membrane flexural stiffnesses due to the piezoelectric coupling within the piezoelectric material, as discussed for piezoelectric beams in [15].

#### 3.1.2. Variational formulation

The variational formulation is based on the principle of virtual work. It can be shown that the Lagrangian for a piezoelectric material is the kinetic energy minus the electric enthalpy as opposed to the purely elastic problems where the internal energy appears instead of the enthalpy [16]. This is the basis for later formulations [17]. For the static case, the Hamilton's principle reduces to

$$\delta H - \delta W = 0 \tag{6}$$

where $\delta H$ is the virtual variation of the electrical enthalpy and $\delta W$ is the virtual variation of the potential energy due to external applied forces. Considering CLPT, neglecting in-plane virtual displacements and assuming zero residual process stresses, the virtual formulation in Eq. (6) can be expressed as (see [17] for further details) :

$$0 = \int_\Omega \left( M_{xx} \delta S^1_{xx} + M_{yy} \delta S^1_{yy} + M_{xy} \delta \gamma^1_{xy} \right) \mathrm{d}x\mathrm{d}y + \oint_{\Gamma_\Omega} \left( \hat{M}_{nn} \frac{\partial \delta w_0}{\partial \hat{\mathbf{n}}} + \hat{M}_{ns} \frac{\partial \delta w_0}{\partial \hat{\mathbf{s}}} \right) \mathrm{d}s + \int_\Omega q \delta w_0 \mathrm{d}s \tag{7}$$

where $\delta w_0$ is the virtual displacment in z-direction. $\hat{M}_{nn}$ and $\hat{M}_{ns}$ are normal and tangential external stress moments applied over the domain $\Omega$'s outer boundary $\Gamma_\Omega$, respectively. They depend on the type of supports that holds the tunable lens. For the clamped case, the second integral vanishes because of zero displacement and zero slope conditions at the edges. $\hat{\mathbf{n}}$ and $\hat{\mathbf{s}}$ are the normal and tangential unit vectors along the outer boundary $\Gamma_\Omega$, respectively. The third integral is the external work due to a pressure force $q$, which vanishes based on having no external pressure and the sixth assumption previously made, i.e. that the polymer or fluid don't affect the membrane displacement. Thus, the weak formulation can be expressed as

$$\begin{aligned} &\int_\Omega \left\{ \left( D^*_{11} \frac{\partial^2 w_0}{\partial x^2} + D^*_{12} \frac{\partial^2 w_0}{\partial y^2} \right) \left( \frac{\partial^2 \delta w_0}{\partial x^2} \right) + \left( D^*_{12} \frac{\partial^2 w_0}{\partial x^2} + D^*_{22} \frac{\partial^2 w_0}{\partial y^2} \right) \left( \frac{\partial^2 \delta w_0}{\partial y^2} \right) \right. \\ &\left. + \left( 2 D^*_{66} \frac{\partial^2 w_0}{\partial x \partial y} \right) \left( 2 \frac{\partial^2 \delta w_0}{\partial x \partial y} \right) \right\} \mathrm{d}x\mathrm{d}y = -\overline{e}_{31} V_\mathrm{p} \overline{z}_\mathrm{p} \int_{\Omega_\mathrm{p}} \left\{ \left( \frac{\partial^2 \delta w_0}{\partial x^2} \right) + \left( \frac{\partial^2 \delta w_0}{\partial y^2} \right) \right\} \mathrm{d}x\mathrm{d}y \\ &= -\overline{e}_{31} V_\mathrm{p} \overline{z}_\mathrm{p} \int_{\Omega_\mathrm{p}} \nabla^2_{x,y} \delta w_0 \mathrm{d}x\mathrm{d}y \end{aligned} \tag{8}$$

Optics EXPRESS

where $\Omega = \Omega_{gl} \cup \Omega_p$. $\Omega_{gl}$ and $\Omega_p$ are domains for glass and piezoelectric layers, respectively. The quantities $D^*_{ij}$ vary over the plate due to the difference in layer structure between the lens pupil and the actuator area. To simplify numerical integration, they can be expressed as

$$D^*_{ij} = D^{\mathrm{gl}}_{ij} + \begin{cases} D^{\mathrm{p}}_{ij}\left[\Pi(X,Y) - \mathrm{circ}\left(\frac{r}{\gamma}\right)\right] & \text{Case I actuator} \\ D^{\mathrm{p}}_{ij}\left[\mathrm{circ}\left(\frac{r}{\gamma_2}\right) - \mathrm{circ}\left(\frac{r}{\gamma_1}\right)\right] & \text{Case II actuator} \end{cases} \tag{9}$$

where $\gamma_1 = \gamma = 2c_1/a$ and $\gamma_2 = 2c_2/a$ (refer to Fig 2). $X = x/(a/2)$, $Y = y/(a/2)$) and $r = R/(a/2)$ are the normalized cartesian and polar coordinates, respectively. The square function $\Pi(X,Y)$ is 1 if $|X| \le 1 \& |Y| \le 1$ and 0 elsewhere. The circle function $\mathrm{circ}(r)$ [18] is 1 if $r \le 1$ and 0 if $r > 1$.

A direct calculation of Eq. (8) at first appears difficult due to the complexity of the integration domains. However, each subdomain is prismatic with square and circular symmetries of their base faces. Thus, it is helpful to decompose these complex integrals into simpler ones over domains with circular or square shape. Based on Eqs. (9), both sides of Eq. (8) can be decomposed as

$$\Xi^{\mathrm{gl}}_{\square} + \left[\Xi^{\mathrm{p}}_{\square} - \vartheta^{\mathrm{p}}_{\circ,\gamma}\right] = \beta^{\mathrm{p}}_{\square} - \zeta^{\mathrm{p}}_{\circ,\gamma} \qquad \text{Case I actuator} \tag{10a}$$

$$\Xi^{\mathrm{gl}}_{\square} + \left[\vartheta^{\mathrm{p}}_{\circ,\gamma_2} - \vartheta^{\mathrm{p}}_{\circ,\gamma_1}\right] = \zeta^{\mathrm{p}}_{\circ,\gamma_2} - \zeta^{\mathrm{p}}_{\circ,\gamma_1} \qquad \text{Case II actuator} \tag{10b}$$

where $\Xi_{\square}$ and $\beta_{\square}$ denote integrals in normalized cartesian coordinates over a square domain, while $\vartheta_{\circ}$ and $\zeta_{\circ}$ denote integrals in normalized polar coordinates over a circular domain. The normalized radius of the circle is denoted by $\gamma$, $\gamma_1$ or $\gamma_2$ in the subscript. The superscripts denote the layer structures of the domains: "gl" for the glass layer and "p" for the piezoelectric layer. The variational calculation in Eqs 10 have the same spatial dependence over the plate as the flexural stiffnesses in Eqs 9. For example, the left hand side of Eq. (10) is the electric enthalpy of the stacked glass and piezoelectric layers over the whole plane minus the electric enthalpy of a circular piezoelectric layer with normalized radius $\gamma$ covering the pupil area. By this construction, we obtain the electric enthalpy stored in the case-I structure. In the same manner, the right hand side is the equivalent force due to the piezoelectric coupling for a rectangular piezoelectric layer extending over the entire diaphragm minus the equivalent force of a circular piezoelectric layer with normalized radius $\gamma$ covering the pupil area. This decomposition method was previously employed in determining approximations for the vibration frequency of rectangular diaphragms with rectangular cuts [19]. Here, we employed it instead for circular cuts and took into account the additional complications of piezoelectric coupling.

#### 3.1.3. Solution of the variational problem

To solve Eq. (8) for the deflection $w_0$ , we write an approximate solution $w_N$ as a finite linear combination of basis functions

$$w_0(X,Y,0) \approx w_N(X,Y,0) = \sum_{m=1}^{N}\sum_{n=1}^{N} C_{mn}\Phi_{mn}(X,Y) \tag{11}$$

where $\Phi_{mn}(X,Y)$ are the basis functions and $C_{mn}$ are coefficients to be determined. The choice of basis functions is an important part of the ansatz. They must satisfy the mechanical boundary conditions. In addition, they should preferably be orthogonal and easy to be mapped to Zernike polynomials [9]. Zernike polynomials are orthogonal polynomials over a disc and are convenient for optical representation of wavefronts. Orthogonality of the basis functions helps eliminating the possibility of a numerically ill-conditioned system of equations arising from the variational treatment. There are many options for the bases, such as products of trigonometric and hyperbolic

Optics EXPRESS

functions [20] known for doubly-clamped beam or products of squared cosines [21]. The disadvantage of the latter functions is that they are not orthogonal.

Moreover, for either of these choices, power series expansions of the basis functions in terms $X$ and $Y$ must be made in order to map to Zernike polynomials. This expansion increases the calculational burden necessary to avoid significant errors from the mapping. Thus, we propose a weighted product of Gegenbauer [22] polynomials on the interval $[-1, 1]$. They are orthogonal and have a simple mapping to Zernike polynomials as will be discussed later. These basis functions can be written

$$\Phi_{mn}(X,Y) = \phi_m(X)\phi_n(Y) = \underbrace{(1-X^2)^{\frac{(\alpha-1/2)}{2}}(1-Y^2)^{\frac{(\alpha-1/2)}{2}}}_{\text{Weight factor enforcing BC}} G_m^{(\alpha)}(X)G_n^{(\alpha)}(Y) \tag{12}$$

where $G_m^{(\alpha)}(X)$ is a Gegenbauer polynomial of order $m$ and the parameter $\alpha$ in the weighting factor should equal $9/2$ to force the basis functions to satisfy the clamped boundary conditions of zero deflection and zero slope along the edges. Due to the symmetry, we will only consider even polynomials, i.e. only functions with both indices $m$ and $n$ even. Figure 3 shows the x-cross section of the first six even basis functions of weighted Gegnenbauer polynomials $\phi_m(X)$. By backsubstituting from Eq. (11) in Eq. (8), we get a linear system of equations for $C_{mn}$ on the form [12]:

$$\underset{N^2\times N^2}{[R_{mnpq}]}\underset{N^2\times 1}{[C_{mn}]} = \underset{N^2\times 1}{[F_{pq}]} \tag{13}$$

where $[R_{mnpq}]$ and $[F_{pq}]$ are calculated using the decomposition described above. A simple way to calculate the integrals is described in the appendix.

The products of finite order Gegenbauer polynomials inside a circle of radius $\gamma = 2c/a$ can be expressed as a linear combination of Zernike polynomials with coefficients depending on the geometrical parameter $\gamma$. For example, the first basis function can be expressed as

$$\begin{aligned}
\Phi_{00}(r,\theta) &= \sum_{i=0}^{N_s}\sum_{j=0}^{N_s} k_{mnij} Z_i^j(r,\theta) \\
&= \left(\frac{3\gamma^8}{640} - \frac{\gamma^6}{16} + \frac{5\gamma^4}{12} - \gamma^2 + 1\right) Z_0^0 + \frac{\gamma^2}{320}\left(3\gamma^3 - 36\gamma^4 + 200\gamma^2 - 320\right) Z_2^0 \\
&+ \frac{\gamma^4}{1344}\left(9\gamma^4 - 84\gamma^2 + 280\right) Z_4^0 + \frac{\gamma^4}{672}\left(-15\gamma^4 + 140\gamma^2 - 168\right) Z_4^4 \\
&+ \frac{\gamma^6}{1280}\left(3\gamma^2 - 16\right) Z_6^0 + \frac{\gamma^6}{384}\left(-3\gamma^2 + 16\right) Z_6^4 + \frac{3\gamma^8}{8960} Z_8^0 - \frac{\gamma^8}{896} Z_8^4 + \frac{\gamma^8}{128} Z_8^8
\end{aligned} \tag{14}$$

where $Z_i^j$ are Zernike polynomials. $N_s = m + n + 8$ is the order of Zernike polynomials sufficient for mapping exactly, $m, n$ are the orders of the basis function $\Phi_{mn}$. Moreover, based on the mirror symmetries of the problem under study, we note from Eq. (14) that we have only even Zernike-polynomial terms in the expansion. Due to this feature, we have an exact representation of the lens surface in terms of Zernike polynomials.

#### 3.1.4. Variational solutions versus FEM

We consider glass as a material for the transparent diaphragm and the PZT stack in [23] for the piezoelectric actuator. Their dimensions and material properties are listed in the appendix. Figure 4(a) shows how the variational solutions for case I match with FEM simulations. To check the convergence of the variational solution to the FEM solution $w_{\text{FEM}}$, we choose to monitor the $l_2$ relative error norm

$$\epsilon_{l_2} = \sqrt{\frac{\sum(w_{\text{FEM}} - w_N)^2}{\sum w_{\text{FEM}}^2}}. \tag{15}$$

Optics EXPRESS

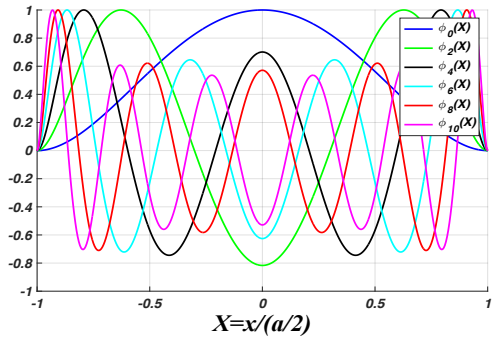


Fig. 3. Even Gegenbauer-polynomial basis functions $\phi_m(X)$ on $[-1, 1]$.

As shown in Fig. 4(b), the error and convergence speed depend on the ratio $\gamma$. For example for $\gamma = 0.1$, the variational solution shows large deviation from FEM solution, especially with a small number of basis functions. The reason is that the spatial frequency of the basis function $\Phi_{mn}$, not to be confused with spatial frequency of light intensity at object plane in the optics part, has to be high enough to capture the displacement. The higher the number of basis functions, the better the solution accuracy. From Figs 4(a) and 4(b), the variational solutions have relative error norms less that 10% at $N = 28$. Thus, they provide good prediction for deflections for case I to be used in optical simulations.

It is evident from Fig. 5 that the variational solutions in case II have similar behaviour as the FEM results, but the error is larger than for case I. The thin-film approximation allows us to use one set of continuous basis functions over the entire square diaphragm. For the case-I actuator, this basis is artificially smooth at the rim of the glass opening where the layer structure changes from glass only to glass and piezoelectric. For the case-II actuator, we have this feature both at the inner and outer perimeter of the piezoelectric ring. For the simpler radially symmetric cases III and IV that will be treated in the next subsection, the plate equations are solved exactly and show very good agreement with FEM.

As shown in Fig. 5(b), it is apparent that having $\gamma_2 \leq 0.5$, the displacement in the circular aperture area becomes nearly flat and it becomes a poor refractive surface adding no optical power to the passing light. Such behaviour is suitable to operate the structure as a piston micromirror as in [24].

The presented modeling framework provides a fast tool, compared to FEM, to perform optimization and exploration of different materials and different layer thicknesses.

### 3.2. Circular diaphragm

Instead of using variational methods for the two piezoelectric actuator configurations in Fig. 2(c) and Fig. 2(d), we rely on previous results in [10, 11] on analytical formulas for the deflection of a multi-layered circular diaphragm. Starting from CLPT and using axisymmetry assumptions, the deflection inside the opening $w_{int}$ can be expressed only in terms of the radial distance $R$ as

$$w_{int}(R) = C_2 R^2 + C_0 = \underbrace{\frac{C_2 \gamma^2 (a/2)^2}{2\sqrt{3}}}_{k_{20}} \underbrace{\sqrt{3}(2r^2 - 1)}_{Z_2^0} + \underbrace{C_0 + \frac{C_2 \gamma^2 (a/2)^2}{2\sqrt{3}}}_{k_{00}} \tag{16}$$

where $C_2$ and $C_0$ are coefficients of $R^2$ and $R^0$ terms, respectively. They are dependent on the driving voltage $V_p$ and their values arise from solving Eq. (36) in [10] and Eq. (14) in [11] for piezoelectric actuator of case III and case IV, respectively. $k_{00}$ and $k_{20}$ are the piston and

Optics EXPRESS

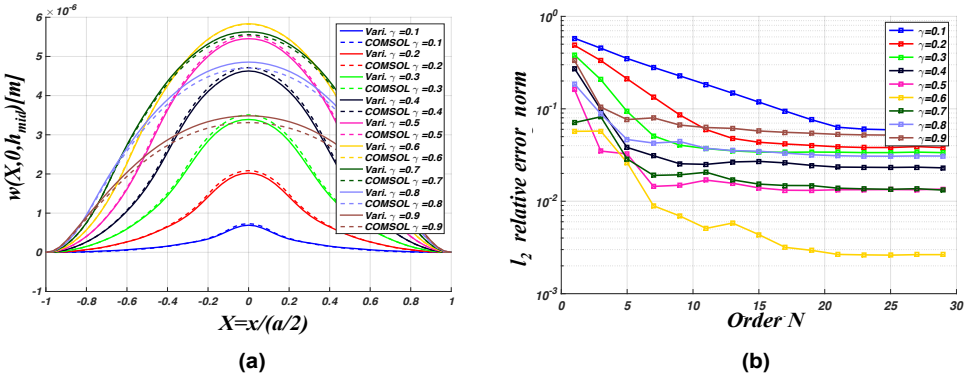


Fig. 4. (a) Displacement profiles in $xz-$plane from FEM and the variational tool ($N = 28$) for square diaphragm with case I actuator at different values of ratio $\gamma$ for piezoelectric material at $V_p = -10V$. (b) $l_2$ relative error norm versus polynomial order $N$.

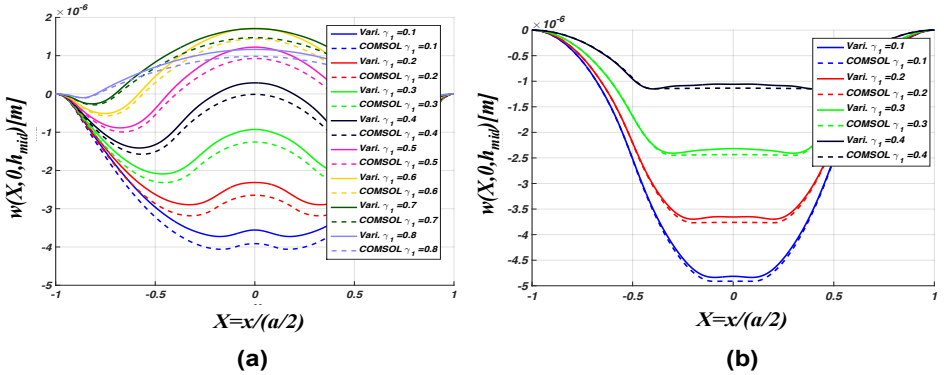


Fig. 5. Displacement profiles in $xz-$plane from FEM and the variational tool ($N = 28$) for square diaphragm with case II actuator at different values of ratio $\gamma_1$ when (a) $\gamma_2 = 0.9$ and (b) $\gamma_2 = 0.5$ at $V_p = -10V$.

defocusing coefficients of the standard Zernike polynomials [9], respectively. $r = 2R/a$ is the normalized radial distance and $\gamma$ ($= \gamma_1$ in case II) is the ratio of the aperture radius to the circular diaphragm radius. The deflection inside the opening is a perfect circular paraboloid.

Figure 6 shows excellent agreement between the results on membrane deflection for the analytical model and the FEM simulations. This is expected since the analytical model is an exact result of CLPT whose assumptions are very good for the thin diaphragms studied here. Similarly to case II, for $\gamma_2 \leq 0.5$, the displacement for case IV in the aperture area becomes nearly flat so that it becomes a poor refractive surface adding no optical power to the passing light. However, it has less stroke-down when compared to case II.

## 4. Optical performance using ray tracing analysis

We perform ray tracing analysis using Zemax [25]; an optical simulation tool. We assume that the glass and polymer (or fluid) layers have a unity optical amplitude transmittance within the visible light range and that their refractive index is equal to 1.5. For ray tracing analysis in Zemax, the tunable lens's entrance pupil opening is uniformly illuminated by parallel rays. Moreover, the entrance pupil is set as a stop surface limiting the ray bundle entering the lens.

Optics EXPRESS

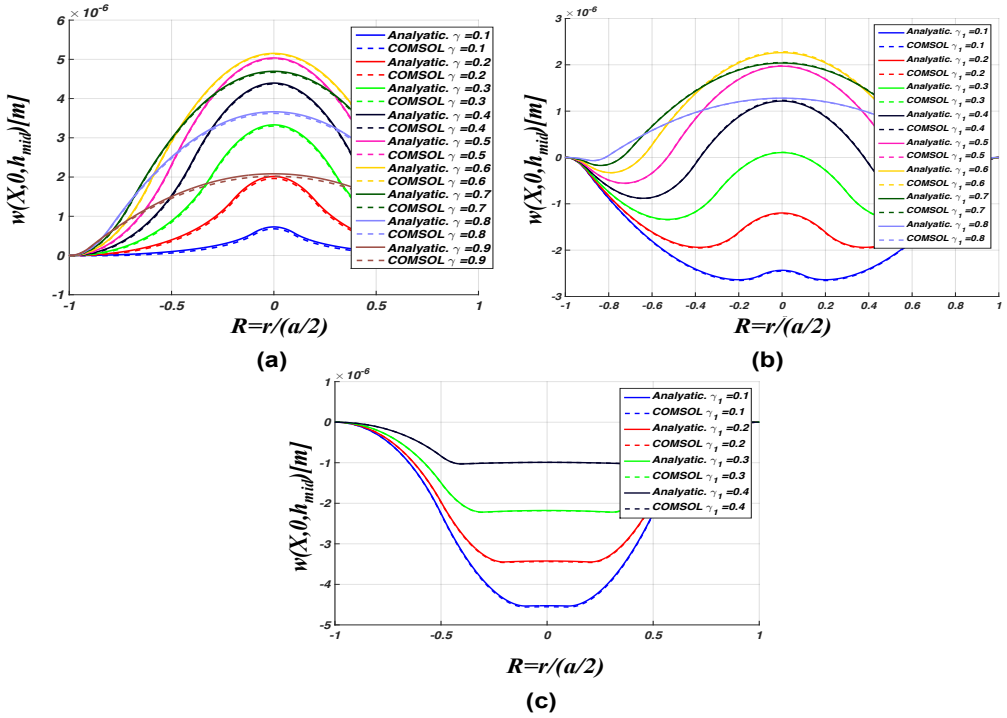


Fig. 6. Displacement profiles in $xz-$plane at $V_p = -10V$ from FEM and the analytical model for (a) case III actuator at different values of $\gamma$ and (b) and (c) case IV actuator at different values of $\gamma_1$ while $\gamma_2$ equals to 0.9 and 0.5, respectively.

In the following, we limited our attention to on-axis optical performance and whenever we use the term 'focal length', we mean the distance from the lens' flat face to the minimum spot. We don't use the paraxial approximation. The lens sag is imported in Zemax using standard Zernike coefficients [9] that are calculated using the Gegenbauer-Zernike mapping, see *e.g.* Eq. (14). However, we imported a $512 \times 512$ grid of surface sag from FEM simulations for case II due to the non-negligible error between variational tool and FEM in that particular case. Surface sag representation with Zernike coefficients enables an easy expression for RMS wavefront error [9]:

$$\sigma_w = \sqrt{\sum_{j=2}^{\infty} a_j^2} \tag{17}$$

where $a_j$ are the coefficients of single index Zernike polynomials. This quantity is a measure of the deviation of the wavefront from a reference sphere having its center at the image plane and a radius equal to the separating distance between the exit pupil position and the image plane, as simulated in Zemax.

### 4.1. Design criterion: minimum $F\#$

A quantitative figure of merit for tunable lenses is the minimum achievable $F\# = f/(\gamma a)$ with acceptable RMS wavefront error. Thus, using the developed tool, we search for the best set of geometrical parameters ($\gamma_1$ or $\gamma$) and $\gamma_2$ to reach this end target. Figure 7(a) shows the arrangement used in Zemax to determine the focal length and RMS wavefront error for the tunable lens. The simulated results in Fig. 7(b) for the square diaphragm (case I ) with $\gamma = 0.57$

gives a minimum F-number of 129 with an RMS wavefront error of 0.0137 waves. For a circular diaphragm (case III), the minimum is $F\# = 136$ and is achieved for $\gamma_1 = 0.54$ and $\gamma_2 = 1$ with a negligible RMS wavefront error, as listed in Tab. 1. Note that the focusing capability of a clamped square diaphragm (case I with $a = 3\ mm$) lies in between the focusing capability of clamped circular diaphragms having radii equal to the inscribed (case III with $a = 3\ mm$) and circumscribed (case III with $a = 3\sqrt{2}\ mm$) circles of the square frame. However, it has a wider aperture that allows a wider ray bundle to enter the lens.

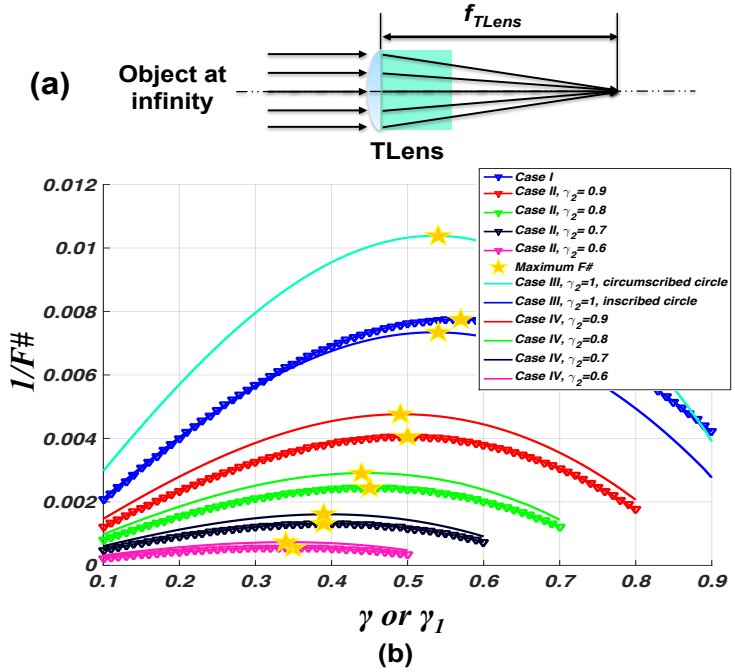


Fig. 7. (a) Tunable lens arrangement for on-axis optical simulation. (b) Reciprocal $F\#$ versus ratio ($\gamma$ or $\gamma_1$) for all tunable lense cases and different $\gamma_2$, all with $V_p = -10V$ and $\lambda = 550nm$.

Table 1. Table contains minimum $F\#$ at different geometrical parameter of PZT actuators at $V_p = -10V$. The optimum cases for square and circular diaphragms are written in bold font.

| | **Square diaphragm** | | | | | **Circular diaphragm** | | | | |
|---|---|---|---|---|---|---|---|---|---|---|
| | **Case I** | **Case II** | | | | **Case III** | **Case IV** | | | |
| $\gamma_2$ | | 0.9 | 0.8 | 0.7 | 0.6 | | 0.9 | 0.8 | 0.7 | 0.6 |
| $\gamma_1$ ($\gamma$) | **0.57** | 0.5 | 0.45 | 0.39 | 0.35 | **0.54** | 0.49 | 0.44 | 0.39 | 0.34 |
| $F\#$ | **129** | 247 | 409 | 759 | 1800 | **136** | 210 | 343 | 622 | 1367 |

Figure 8 shows the achievable focusing range ($\infty$ to 22.1 cm) and ($\infty$ to 22.3 cm) with optimum geometrical parameters for case I and case III, respectively, as the voltage is varied from 0 to $-10$ V. However, case I achieves slightly lower $F\#$ and wider aperture. The voltage was limited to $-10V$ to comply with the assumptions that the deflection is mainly due to bending and that nonlinear coupling is insignificant. The square diaphragm suffers from an RMS wavefront error which depends linearly on the voltage. This linear dependency is due to having the displacement profiles, by assumption, linearly dependent on voltage. As a consequence, so are the Zernike

coefficients. This causes the RMS wavefront error to be linearly dependent on the voltage. However, the RMS wavefront error is still less than 0.0137 waves over the focusing range.

For the optimum of case I, the opening diameter is 1.71 mm and the wavefront error, as shown in Fig. 8(b) is dominated by the Zernike-quadrafoil aberration $Z_4^4$ and arises from clamping the frame at the four corners. For the optimum of case III, the opening diameter is 1.62 mm, which is less than for case I, and the wavefront error is negligible, as shown in Fig. 8(c), so that it can be neglected. This nearly zero RMS wavefront error is due to having the lens sag, from Eq. (16), as a symmetric circular paraboloid, which will be very similar to a sphere when the exit pupil transverse dimension is much less than the reference sphere's radius. It seems that having a square diaphragm reduces the effect the clamped edges allowing larger displacement at the diaphragm centre. This contributes to a relative enhancement in the focusing capability and enables lower $F\#$ compared to the circular diaphragm. The introduced RMS wavefront error in case I is very small compared to $\lambda/14$, as in Maréchal's criterion [26] that judge the deviation from diffraction-limited performance.

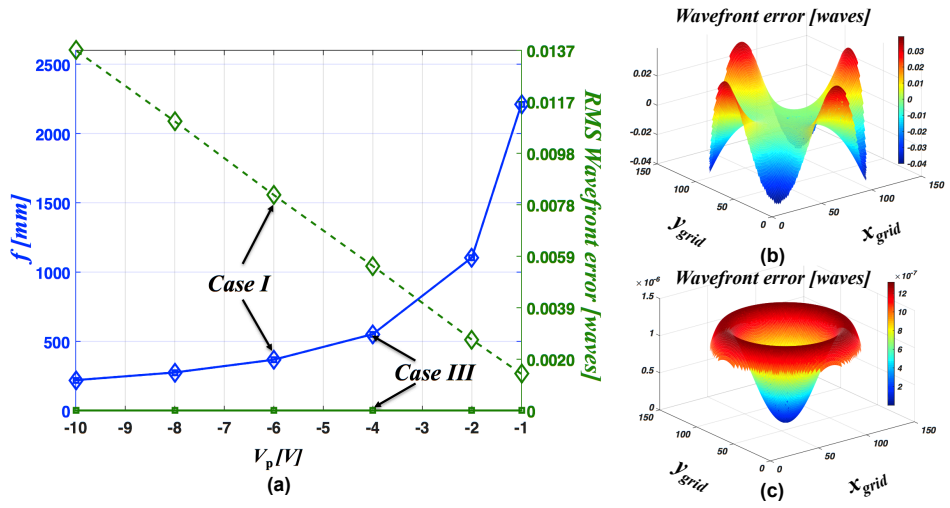


Fig. 8. (a) Focal length $f$ and RMS wavefront error versus applied voltage on the piezoelectric stack with optimum geometrical values for tunable lens for square/circular diaphragm. Wavefront map using exit pupil shape at $V_p = -10V$ for (b) square and (c) circular diaphragm.

### 4.2. *Tunable lens with a paraxial fixed lens*

Figure 9(a) shows the tunable lens arrangement with an ideal fixed lens having $F\# = 2.8$ positioned at the tunable lens's exit aperture. This fixed lens was modeled using the paraxial approximation ($\sin\theta \approx \theta$) so that it does not introduce aberrations of its own. Its entrance-aperture dimension equals to the tunable lens's opening diameter. This layout enable us to put the object at different focus positions, based on the actuation voltage $V_p$ and monitor MTF at the image sensor. The sagittal MTF and tangential MTF are the same due to the symmetry of

our cases. Figures 9(b) shows that the overall spatial cutoff frequency remains the same for all voltages for both the circular and square diaphragm. Due to the tunable focus feature, the capability of capturing details remains unchanged for any object distance from the combined optical system of tunable lens and fixed lens. A closer look at the MTF passband shows that MTFs for case I at ($V_p < -4V$) drop a little from the diffraction-limit behavior due to the wavefront error. However, the MTF for case III perfectly matches with the diffraction limited MTF at different voltages due to the negligible wavefront error. In more realistic simulations, a real fixed lens with its own aberrations will be placed after the tunable lens and the MTF will be evaluated at different object distances.

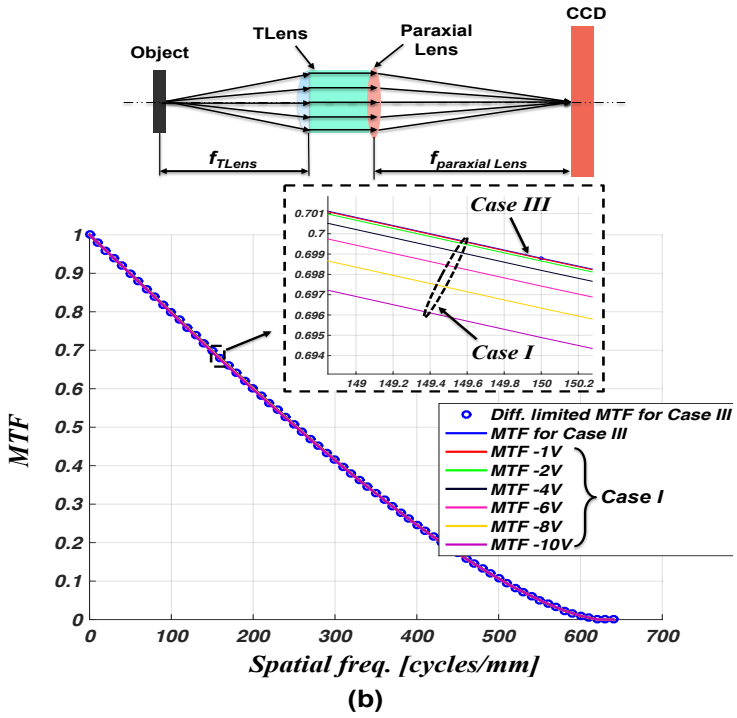


Fig. 9. (a) Arrangement of tunable lens with a paraxial fixed lens and image sensor in Zemax for on-axis optical simulation. Sagittal (tangential) MTF at image plane for tunable lens for optimum cases I and III at different actuation voltage $V_p$.

## 5. Conclusion

The presented modeling framework effectively predicts the linear static opto-electromechanical performance of different actuator configurations for piezoelectrically actuated tunable lenses under the assumptions of classical laminated-plate theory, linear theory of piezoelectricity, quasi-electrostatic condition, a thin film approximation and ray tracing. It provides a fast design tool for complicated study cases that involve both square and circular symmetries. Its accuracy, when compared to FEM, depends on the number and boundary of transitions between areas that are covered by a piezoelectric film and those that aren't. It is fast due to the simple proposed numerical representation of variational integrals and the accurate analytic mapping equations from Gegenbauer product polynomials to Zernike polynomials with no residues. The predicted deflection from the electromechanical stage in our modelling framework can be used whenever the relative error norm is less that 10%. The modeling framework can be utilized for the

Optics EXPRESS

optimization of different material choices and layers thicknesses to find the optimum ratio $\gamma$.

We found out that the circular actuator with a circular opening on the circular diaphragm can achieve 5 diopters with a 10-V voltage source and has negligible RMS wavefront error because of the symmetric paraboloid sag shape that is close to reference sphere at the image plane. However, the square actuator with a circular opening on the square diaphragm reaches the same 5 diopter with the same 10-V voltage source with a slightly wider aperture and has a RMS wavefront error less than the Maréchal's criterion. Their on-axis MTFs, in combination with a paraxial lens, remain essentially diffraction-limited for different object distances through tuning the actuation voltage. This effectively changes the overall focal length to focus at different object planes while still having the same resolution.

## 6. Appendix

### 6.1. Materials

In the analyzed structures, we consider glass as the transparent layer and {100}-textured $PbZr_{0.53}Ti_{0.47}O_3$ thin film [23] as the piezoelectric material. The PZT stack is $2\mu m$ thick and has a 100 nm bottom electrode from Pt {100} grown on 10 nm thick $Ti/TiO_2$ adhesion layers. Platinum electrodes and adhesion layers are neglected in calculations due to their small thicknesses compared to both glass and PZT layers. Material properties are listed in Table 2. The circular-diaphragm diameter and the side length of the square diaphragm are both $a$ = 3mm.

Table 2. Table contains values for PZT and glass material parameters.

| $PbZr_{0.53}Ti_{0.47}O_3$ **thin film** | | | | | Glass |
|---|---|---|---|---|---|
| $h_{\mathrm{p}} = 2\mu m$ | | | | | $h_{\mathrm{gl}} = 20\mu m$ |
| $S_{11}^E$ | $S_{12}^E$ | $S_{13}^E$ | $S_{33}^E$ | $S_{44}^E$ | E |
| 13.8 $pPa^{-1}$ | -4.07 $pPa^{-1}$ | -5.8 $pPa^{-1}$ | 17.1 $pPa^{-1}$ | 48.2 $pPa^{-1}$ | 44 GPa |
| $S_{66}^E$ | $d_{31}$ | $d_{33}$ | $d_{15}$ | $\epsilon_{33}^S/\epsilon_0$ | $\nu$ |
| 35.74 $pPa^{-1}$ | -116.8 $pm/V$ | 224.2 $pm/V$ | 330 $pm/V$ | 854.7 | 0.2 |

### 6.2. Effective parameters

Classical laminted plate theory assumes a plane stress condition ($S_{zz} = 0$). Thus, an elimination of stress component $T_{zz}$ from the constitutive equations, results in effective material parameters

$$\overline{Q}_{ij} = \overline{C}_{ij}, \quad \overline{C}_{11} = \frac{s_{11}^E}{\left(s_{11}^E + s_{12}^E\right)\left(s_{11}^E - s_{12}^E\right)}, \quad \overline{C}_{12} = \frac{-s_{12}^E}{\left(s_{11}^E + s_{12}^E\right)\left(s_{11}^E - s_{12}^E\right)} \tag{18a}$$

$$\overline{C}_{66} = \frac{1}{s_{66}^E}, \quad \overline{e}_{31} = \overline{e}_{32} = \frac{d_{31}}{s_{11}^E + s_{12}^E}, \quad \overline{\epsilon}_{33}^S = \epsilon_{33}^S - \frac{2d_{31}^2}{s_{11}^E + s_{12}^E} \tag{18b}$$

### 6.3. Closed form for integrals

To determine the integrals involving the Gegenbauer polynomials, we use the definition of the polynomials and two recurrence identities [22]:

Optics EXPRESS

$$G_n^{(\alpha)}(X) = \sum_{k=0}^{\lfloor n/2 \rfloor} \frac{(-1)^k \Gamma(n-k+\alpha)}{\Gamma(\alpha) k!(n-2k)!} (2X)^{n-2k}, \tag{19}$$

$$(2\alpha + i) G_i^{(\alpha)}(X) = (i+1) X G_{i+1}^{(\alpha)}(X) + 2\alpha(1-X^2) G_i^{(\alpha+1)}(X), \tag{20}$$

$$\frac{\partial G_i^{(\alpha)}(X)}{\partial X} = 2\alpha G_{i-1}^{(\alpha+1)}(X). \tag{21}$$

Based on these identities, the first and second derivatives of the weighted Gegenbauer polynomial $\phi_i(X)$ are

$$\frac{\partial \phi_i}{\partial X} = (1-X^2)^{\frac{(\alpha-5/2)}{2}} \left[ -(\alpha + i - 1/2) X G_i^{(\alpha)}(X) + (2\alpha + i - 1) G_{i-1}^{(\alpha)}(X) \right], \tag{22}$$

$$\begin{aligned} \frac{\partial^2 \phi_i}{\partial X^2} = (1-X^2)^{(\frac{\alpha-9/2)}{2}} \Big[ & (\alpha + i - 1/2) \left( (\alpha + i - 3/2) X^2 - 1 \right) G_i^{(\alpha)}(X) \\ & - (2\alpha + i - 1)(2\alpha + 2i - 4) X G_{i-1}^{(\alpha)}(X) + (2\alpha + i - 1)(2\alpha + i - 2) G_{i-2}^{(\alpha)} \Big]. \end{aligned} \tag{23}$$

The product of first derivatives can be written as

$$\begin{aligned} \frac{\partial \phi_i}{\partial X} \frac{\partial \phi_p}{\partial X} = (1-X^2)^{(\alpha-5/2)} \Big[ & (\alpha + i - 1/2)(\alpha + p - 1/2) X^2 G_i^{(\alpha)}(X) G_p^{(\alpha)}(X) \\ & + (2\alpha + i - 1)(2\alpha + p - 1) G_{i-1}^{(\alpha)}(X) G_{p-1}^{(\alpha)}(X) - (\alpha + i - 1/2)(2\alpha + p - 1) X G_i^{(\alpha)} G_{p-1}^{(\alpha)} \\ & - (\alpha + i - 1/2)(2\alpha + i - 1) X G_{i-1}^{(\alpha)} G_p^{(\alpha)} \Big]. \end{aligned} \tag{24}$$

Thus, in general the integrals will be on the form

$$\int (1 - 2X^2 + X^4) X^\beta G_i^{(\alpha)}(X) G_p^{(\alpha)}(X) \mathrm{d}X = \mathbf{W}^T \mathbf{X} \tag{25}$$

where the $k^{th}$ elements for the $m \times 1$ matrices $W$ and $X$ can be written

$$W_{(k)}(l,s) = \frac{(-1)^{l+s} \Gamma(i-l+\alpha) \Gamma(p-s+\alpha)}{[\Gamma(\alpha)]^2 l!(i-2l)! s!(p-2s)!} (2)^\eta \tag{26a}$$

$$X_{(k)}(l,s) = X^{\eta+\beta+1} \left[ \frac{1}{\eta+\beta+1} - \frac{2X^2}{\eta+\beta+3} + \frac{X^4}{\eta+\beta+5} \right] \tag{26b}$$

where

$$m = (\lfloor i/2 \rfloor + 1)^{(\lfloor p/2 \rfloor + 1)}, \quad \eta = i + p - 2(l+s), \tag{27}$$

$$l = 0, 1, ..., \lfloor i/2 \rfloor, \quad s = 0, 1, ..., \lfloor p/2 \rfloor \quad \text{and} \quad k = 0, 1, ..., m. \tag{28}$$

## Futurework

We plan to include the nonlinear behavior in the variational formulation and study the tunable lens performance in combination with a fixed lens made for a mobile phone.


## Funding

Research Council of Norway (no. 235210).

## Acknowledgments

The authors thank the Research Council of Norway and PoLight for financial support.